fractal and fractional

MDPI

Article

Multivariate Analysis on a Complex, Rare-Earth Doped Alumina Database with Fractal Dimension as a Microstructural Quantifier

Zeno Dorian Ghizdavet [1], Adrian Volceanov [1,*] and Enikő Volceanov [2]

[1] Department Science and Engineering of Oxide Materials and Nanomaterials, Faculty of Chemical Engineering and Biotechnologies, University POLITEHNICA of Bucharest, 313 Splaiul Independentei, 060042 Bucharest, Romania; zeno.ghizdavet@upb.ro
[2] Metallurgical Research Institute, ICEM SA, 39 Mehadia, 060054 Bucharest, Romania
* Correspondence: adrian.volceanov@upb.ro

Abstract: Alumina ceramics were obtained from three different alumina sources, A1–A3, with various rare-earth dopants (La_2O_3–La, Nd_2O_3–Nd, and Y_2O_3–Y), concentration levels (500 and 1000 ppm) and synthesizing routes (1500 °C, 1815 °C and cold plasma-P). Absorption (A) and density (ρ in text, rho in images) were measured, resulting in a complex, multivariate database. Principal Component Analysis (PCA) was run with the aim of deducing relationships between variables (alumina source, dopant level, thermal processing route, A and ρ), observations, and between variables and observations. A total of 206 Scanning Electron Microscopy (SEM) micrographs were recorded at various scales and the corresponding images were processed to quantify the microstructural features. Two techniques of edge detection were used; Fractal Dimension (FD) was calculated for each micrograph and results were compared. Various scales of the micrographs prevented us from using any other approach, such as simply measuring the grains or obtaining shape parameters. The initial database was extended by including FDs and PCA was run again. We found that plasma processing is positively correlated to A and negatively correlated to both temperature (T) and ρ; La ceramics have an opposite behavior to Y and Nd ceramics. FD successfully explained observations being correlated, mainly, to Y, Nd and, to a lesser extent, to La. FD proved that it is a reliable and simple approach to quantifying microstructural features when comparing highly different, noisy micrographs.

Keywords: fractal dimension; multivariate analysis; image processing; alumina; sintering; dopants

Citation: Ghizdavet, Z.D.; Volceanov, A.; Volceanov, E. Multivariate Analysis on a Complex, Rare-Earth Doped Alumina Database with Fractal Dimension as a Microstructural Quantifier. *Fractal Fract.* **2023**, *7*, 286. https://doi.org/10.3390/fractalfract7040286

Academic Editor: Haci Mehmet Baskonus

Received: 23 February 2023
Revised: 17 March 2023
Accepted: 23 March 2023
Published: 26 March 2023

1. Introduction

The structural ceramic materials resistant to high temperatures, exhibiting impressive series of mechanical properties, including excellent mechanical strength in extreme conditions are of great importance being usually lightweight, and harder than metals. The alumina-based materials and composites are among the top high-tech applications. On the other hand, sintering, and densification of high-grade alumina and related high alumina content composites is still a challenging matter. The sintering behavior of three types of high-grade alumina prepared from various precursors using different techniques when doped with lanthanide oxides (Ln_2O_3, Ln = Y, Nd, and La) is analyzed through the resulting microstructural features. Grain-boundary diffusion is expected as the dominant densification mechanism for pure and doped alumina [1–3]. The use of rare-earth dopant systems has had the purpose of better understanding the role of oversized, isovalent cation dopants in determining expected ceramic and mechanical properties [4,5]. The effect of the dopants is believed to be linked strongly to their segregation at the Al_2O_3 grain boundaries, employing complex diffusion mechanisms. In these circumstances, only a complex statistical analysis [6] can emphasize the microstructural features of various alumina types

sintered under completely different conditions (heat transfer mechanisms), but similar doping levels.

Microstructural features should be assessed to identify correlations in the chain: materials, composition, processing, microstructure, and properties; various approaches are available. A simple one, used in [7], was to obtain the average grain size of Nd-doped alumina ceramics from fracture surfaces by measuring >300 grains in multiple micrographs at random locations and relating the average grain size to optical properties. It was, also, revealed on elemental maps for Al, O, and Nd in TEM micrographs with energy-dispersive X-ray spectroscopy that Nd dopant could be found within the matrix but also along grain boundaries and triple points. The linear intercept method was used in [8] to compute the mean grain size of rare-earth-doped transparent alumina ceramics and to identify the dependence of real in-line transmittance on the mean grain size. It was demonstrated in [9] that digital image processing with edge detection can be applied in particle size analysis in aggregate processing plants. Shape factors are well-known to characterize granular materials, to numerically describe the shape of a particle; still, they have their limitations [10,11].

All these approaches could work when there is a clear grain/pore boundary that can be digitally processed; however, when dealing with microstructures obtained at various scales, features are also different, and they cannot be obtained and compared in an identical way. The fractal dimension calculation is an approach that is independent of the scale and feature diversity; therefore, it was used on processed SEM images.

Fractal dimension is used in Image Processing extensively, with a broad area of applications when a measure of the degree of geometric irregularity is needed. Theory, areas of application, and methods used to determine the fractal dimension are well covered in literature [12–14] so it will not be detailed here. For a two-dimensional, binary (black/white) image containing at least one curve, FD can vary from 1 to 2; the irregularity of the boundaries/number of black pixels contained in the picture increase when FD increases from 1 to 2. FD can be obtained for boundaries both with Richardson and Box Counting methods [15]. Richardson's method consists of covering the boundary, successively, with sticks of different lengths and counting the resulting findings; thus, it is easier to use on single-grain boundaries rather than on a complicated net of boundaries. The Box Counting method simply counts the number of pixels found in boxes of different areas, thus being more appropriate to analyze SEM images of rough surfaces taken at different magnifications (scale length of 5 to 500 μm).

Box-counting method is highly versatile, so it could be carried in various applications in materials science [10,12,16], in calculating, say, the fractal dimension of Australia's coastline (by implementing a multicore parallel processing algorithm) [17], in medical imaging [18] and to correlate pore volume's fractal dimensions to the strength of high temperature treated cement paste [19]. Fractal dimension was found to be related to the amount of laser-induced defects on photoinduced light scattering patterns in ferroelectric crystals of lithium niobate [20].

Mercury intrusion porosimetry data were used in [13] to obtain the fractal dimension of porous alumina, with FD values ranging from 2.6 to 2.9. FD was negatively correlated with porosity and positively correlated with the bending strength of porous alumina. Fractal dimensions in the range $1.8 < FD < 2.6$ were obtained in [14] from gray-scale SEM micrographs and binary images resulting from median filtering of the original SEM micrographs; strong correlations between roughness parameters and fractal dimension were identified.

The purpose of this work was to identify correlations in the causal chain: materials–composition–processing–microstructure–properties, with multiple choices for each link, method of edge detection, and statistical analysis. Principal Component Analysis helped to understand the data on a scientific basis and to extract correlations, along with some other statistical techniques. The fractal dimension was identified to be an effective quantifier

of highly dissimilar and/or noisy microstructures and the best edge detection technique was selected.

2. Materials and Methods

2.1. Materials

Three alumina sources were successively mixed with three rare-earth dopants in two concentration levels, according to Table 1.

Table 1. Compositional codes and concentration levels of dopants.

Compositional Codes			
Sample	Alumina type	Rare-earth oxide	Level (ppm)
A1La5	A1 (Al_2O_3 from sulphate, 1.2 µm average grain size)	La_2O_3	500
A1La10			1000
A2La5	A2 (Al_2O_3–very fine powder, 325 mesh)	La_2O_3	500
A2La10			1000
A2Y5		Y_2O_3	500
A2Y10			1000
A2Nd5		Nd_2O_3	500
A2Nd10			1000
A3La5	A3 (Al_2O_3 ACS, 2.1 µm average grain size)	La_2O_3	500
A3La10			1000
A3Y5		Y_2O_3	500
A3Y10			1000
A3Nd5		Nd_2O_3	500
A3Nd10			1000

A1 alumina originating from sulfate did not prove to be of interest for applications where small, uniform alumina grains are requested. For this reason, only mixtures of A1 based on La_2O_3 were made for possible comparisons with other types of alumina and sintering methods.

The powder mixtures were shaped in cylinders with 1.32 cm diameter and equal cross heights by uniaxial pressing (150 MPa), then were subjected to thermal treatments at temperatures of 1500 °C for 4 h (electric oven), 1815 °C for 2.5 h (gas furnace), and finally to a non-conventional technique, based on cold plasma for 0.5 h. All details are given in [21].

After sintering, the samples were subjected to the following analysis:

- XRD diffraction analysis–for its mineralogical composition.
- Determination of ceramic properties–absorption and relative density.
- Scanning electron microscopy (SEM) for the fracture morphology of sintered samples.

Density and absorption were determined as follows: The samples are weighted in the air (m_0) on the analytical balance and kept in a vacuum for two hours. They are immersed in xylene, and the vacuum pump is turned off. After 30 min, the saturated samples are weighed in normal pressure conditions. Density and absorption were then calculated with Formulas (1) and (2):

$$\rho_a = \frac{m_p}{V_a}\left(\mathrm{g/cm^3}\right) \quad (1)$$

$$A = \frac{m_s - m_p}{m_p} \cdot 100\,(\%) \quad (2)$$

where ρ_a is relative density, m_p—sample mass, *Va*—sample volume, and m_s—saturated sample mass.

2.2. Principal Component Analysis (PCA)

PCA is a multivariable, versatile technique that can assess, visualize and understand relationships among variables, between observations and variables, and similarities be-

tween observations, to uncover functional patterns in an appropriately sized dataset. PCA can handle variables that are otherwise difficult to analyze and compare, such as variables of different orders of magnitude, of a different nature (in this case, information about composition, processing temperature, microstructural features, properties, etc.), variables that can have discreet values; it is one of the most popular and a highly powerful multivariate statistical technique [22–24]. Variants of the technique have been developed that are tailored to various different data types and structures [23]. PCA was successively used to address multivariate analysis in conjunction with Self-Organizing Maps (SOM) [10,24].

As the technique is widely available, its description will be given in short: original variables will be used to construct new variables, called Principal Components (PCs), made of linear combinations of the original variables. The first PC retains most of the variance in the original dataset, while the subsequent ones most of the remaining variance while being orthogonal to the preceding one(s). Variables and observations are projected on planes made of combinations of PCs, say, a 2D plot of a plane made by PC1 + PC2 (or other combination), instead of being represented in an n-Dimensional space, with n being the number of original variables.

To adequately describe the data and to visualize the existing relationships, variables are plotted as vectors. Vectors that have their length close to the origin (the average point on the projection plane) describe variables with average properties, i.e., no significance (importance) on the PC that they are projected. On the opposite, if a vector is very close to a particular PC axis, its length is at the maximum possible (in absolute value) or close to it, and the corresponding variable will be highly significant on that PC. Intermediate values have intermediate significances. Poorly represented, less essential variables for the model are primarily associated with higher-order PCs.

Variables/observations closely positioned on the projection plane made by any combination of two PCs have a similar behavior/tend to belong to a given group; if opposite, their behavior is dissimilar. Identifying relationships between variables and observation is also a position-driven analysis and requires comparing the positions of the variables and observations in the variables and score plots (scores are coordinate values of the observations along the PC lines).

The issue with PCA is that it is appealing to attempt a detailed, exhaustive interpretation of all variables and small clusters of observations and relationships between them and to identify every possible influence on the results. However, in many, if not most cases, data variability is covered by more than 2 PCs (and some other limitations were identified in [22]), so the interpretation should be limited to the obvious, major findings; otherwise, it may risk being a forced, explanatory-driven analysis. For example, PCA can be misused if the database is adjusted to match existing knowledge [22].

PCA biplots were also used to extract information from variables and observations. In brief, PCA biplots represent variables by axes and observations as points in the same chart, allowing visual extracting relationships between variables, observations, and between variables and observations. For observations, the closer they are, the more similar their behavior is; opposite entities have dissimilar behavior. Axes contain actual values so that the position of the observations on the plot can be attributed, by projection on the axis, to a certain value of the variable. Close axes that have values ordered inversely are still correlated but negatively; the closer they are, the stronger their correlation is.

PCA was conducted with STATISTICA 10 software [25].

2.3. Image Processing

SEM image processing was made in ImageJ scientific software aiming to compute Fractal Dimension. FD was used to quantitatively describe the morphology of the microstructure so that it can be used as an index allowing multivariate statistical analysis, along with alumina source, composition, processing conditions, and ceramic properties. Microstructural features of interest are grain boundaries, various types of pores (both inter and intragranular), fracture planes, and the corresponding resulting edges.

The median filter was also tested in processing the image to remove the existing noise before applying any edge detection technique; it is known that the Median filter preserves [most] of the edges well. The Median is calculated by first sorting all the neighboring pixel values and then replacing the pixel being considered with the median pixel value [26].

To compute FD, images were first converted from RGB format to binary images, and edges of the particles were found. Note that, here, the edge does not mean only grain boundaries but also pore boundaries, edges resulting from fracture planes, etc. Find Edges Tool and Canny Edge Detection plugin were compared to identify and isolate edges. Resulting in 206 images × 2 sets for each edge detection technique used for FD calculation. Find Edges tool uses a Sobel edge detector to highlight sharp changes in intensity in the image [27]. Canny Edge Detection removes, firstly, the noise in the image with a 5 × 5 Gaussian filter, then finds the edge gradient and direction for each pixel and removes any unwanted pixels which may not constitute the edge. The resulting image is thresholded by a minimum and maximum value, thus resulting in clear edges, if the intensity gradient is higher than the maximum value or if they have intermediate values and they are connected to an existing already defined edge, and a possible edge if not [28]. If the value is lower than the minimum thresholding value, it is not an edge.

3. Results and Discussions

3.1. Experimental Results

A complex database resulted from synthesizing alumina from A1–A3; A1 alumina was doped only with La, while A2 and A3 were doped with all three oxides (La, Y, Nd) in two concentration levels (500 ppm–code 5 and 1000 ppm–code 10)—see Table 1.

All 14 resulting combinations were thermally processed via three different routes, two of them being conventional: 1500 °C and 1815 °C, coded 1500 and 1800, respectively; the third one was plasma processing (code P), thus resulting in 42 different ceramics—see Table 2.

Table 2. Ceramic properties (ρ and A) recorded at 1500 °C, 1815 °C, cold plasma.

		1500 °C			1815 °C			Cold Plasma	
Mix	**Item**	**ρ (g/cm^3)**	**A (%)**	**Item**	**ρ (g/cm^3)**	**A (%)**	**Item**	**ρ (g/cm^3)**	**A (%)**
A1La10	1	2.31	20.17	15	3.54	1.57	29	1.549	38.71
A1La5	2	2.56	15.51	16	3.53	0.07	30	1.600	36.61
A2La10	3	2.60	14.82	17	2.62	11.69	31	2.462	14.97
A2La5	4	2.64	13.44	18	3.35	3.44	32	2.355	16.77
A2Nd10	5	2.59	14.41	19	3.07	4.24	33	2.193	20.05
A2Nd5	6	2.58	15.04	20	3.40	1.23	34	1.929	26.19
A2Y10	7	2.62	14.02	21	3.46	0.75	35	2.588	13.28
A2Y5	8	2.62	13.93	22	3.25	2.56	36	2.295	17.82
A3La10	9	3.48	3.11	23	3.45	2.33	37	2.279	18.46
A3La5	10	3.46	3.57	24	2.71	10.35	38	2.104	21.31
A3Nd10	11	3.57	2.12	25	2.36	15.55	39	2.049	22.47
A3Nd5	12	3.43	4.16	26	2.77	9.46	40	2.630	12.61
A3Y10	13	3.53	3.41	27	3.60	0.12	41	2.075	21.81
A3Y5	14	3.55	2.81	28	2.85	8.23	42	2.284	5.16

3.1.1. Ceramic Properties

Two ceramic properties, ρ and A, were measured for all combinations, and SEM images were taken at different scales of observations, from 5 to 500 μm (note that not all scales were used for all combinations).

The experimental results revealed some interesting aspects regarding the sintering behavior of alumina. The first conclusion is that ceramic properties depend on the following:

- heat treatment temperature;
- the type of thermal treatment (see the case of cold plasma);

- the nature of the alumina precursor;
- of the nature and amount of added dopant.

The values of the ceramic properties (absorption and apparent density) are directly influenced by the sintering temperature and the way the thermal transfer is carried out (firing, cold plasma, microwaves) [29–31]. Thus, in Table 2, it can be found that the best sintering behavior at 1500 °C has A3 alumina, regardless of the nature of the sintering dopant (La, Y, or Nd) or its concentration. On the opposite side is alumina A1, which presents the highest absorption values.

The sintering performed at 1815 °C for the same categories of compositions highlighted a more complicated behavior even when using the same dopant. It can be observed that absorption reaches minimum values in the case of all three types of alumina but for different dopants. This random behavior suggests that the sintering mechanism involving different dopants could be different for different oxides and different sintering temperatures.

In the case of using cold plasma, the mechanism of heat transfer from the source to the material is entirely different from the previous traditional issues (gas heating, respectively electric heating). In addition, these results are for the first time, so there is no comparative data for this sintering method from the point of view of working parameters or ceramic properties possible to obtain. As can be seen, absorption values are generally higher than traditional burning methods, confirmed by the porous microstructure observed during SEM determinations. However, the lowest values of absorption were determined in the case of the A3La5 composition, which also showed good behavior in the other sintering conditions.

Cold plasma burning shows the same characteristic: high absorption values for almost all compositions.

One way to estimate the degree of sintering of a ceramic material is the density of the sintered specimens. As expected, the highest density values were recorded for the samples sintered at 1815 °C (almost all pieces had values above 3 g/cm^3). However, high-density values were also recorded for some samples fired at 1500 °C in the case of using type A3 alumina for all dopants and all concentrations used.

This last type of behavior drew attention to the nature of the alumina precursor. By analyzing the density values of samples made with the three types of alumina used, doped with the same concentration of dopant (La_2O_3) and sintered under different conditions, the highest density value was recorded for the A3La10 composition.

3.1.2. X-ray Diffraction Analysis

As expected, X-ray diffraction analyses confirmed the exclusive presence of alumina in the form of α-Al_2O_3 without highlighting any other compound or solid solution of aluminum trioxide with one of the lanthanide oxides used as sintering additives. Lanthanide oxides were preferred as such additions because further studies will be performed on Al_2O_3-SiC type composite materials or other non-oxidic ceramic materials and which, according to some literature data, require the presence of these oxides [5].

3.1.3. Microstructural Characterizations

Scanning electron microscopy (SEM) for the fracture morphology of sintered samples was performed using a scanning electron microscope HITACHI S2600N equipped with a system for energy dispersive analysis (EDS). The micrographs confirmed many assumptions used to explain the sintering behavior based on the ceramic properties data. Only a few analyzed cases will be presented to have a global picture of the studied sintering. Figure 1a shows the micrograph of the A1La10 sample fired at 1500 °C, with an average size of the granules of 2 μm and porous microstructure. The same composition fired at 1815 °C-Figure 1b shows well-developed crystals, with well-defined crystallization planes. However, inside these planes, several pores with a diameter of about 1 μm can be distinguished, probably a consequence of the sintering mechanism and the action of the dopant. The clarification of these aspects requires further studies.

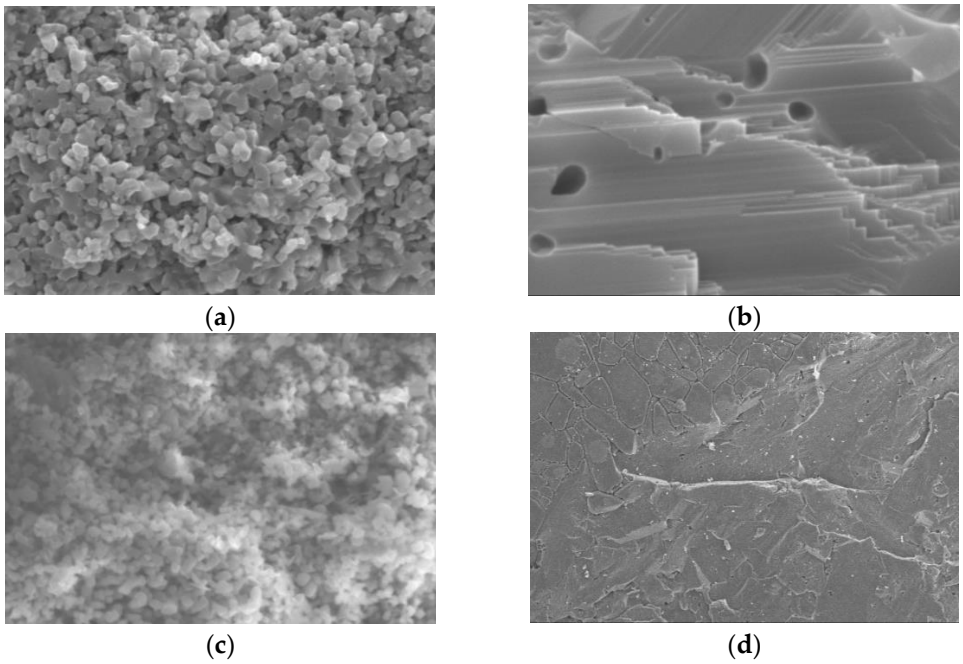

Figure 1. (**a**) A1La5 ceramic processed at 1500 °C, scale 10 μm; (**b**) A1La10 ceramic processed at 1815 °C, scale 50 μm evidences intragranular porosity and fracture planes; (**c**) A1La10 ceramic processed in plasma, scale 10 μm; (**d**) A3La10 ceramic processed at 1815 °C, scale 250 μm, with both compacted areas and grain boundaries.

Figure 1c shows the microstructure of the same A1La10 composition sintered in cold plasma. By the determinations of ceramic properties, the microstructure appears very porous, with submicron grains, presenting a structure similar to sol-gel microstructures.

Conclusively, SEM micrographs showed very different microstructural features, being difficult to compare from one scale to another.

3.2. Principal Component Analysis Results

Experimental data given in Table 2 were analyzed by Principal Component Analysis (PCA). The scree plot showed that 89.65% of the sum of squares has been explained by the first three extracted components (PC 1 accounted for 48.33%, PC 2 for 21.8%). Projection of the variables on Figure 2a PC1 and PC2 plane; (b) PC1 and PC3 plane revealed that data variability is almost entirely described on PC1 by A and P, on one side, and T and ρ, (denoted by rho in the PCA images) on the opposite side. Both groups (A + P) and (T + ρ) have high values, close to 1 on PC1, meaning they are highly influential on this PC. Each group's projections are close, so their behavior can be interpreted similarly. On a factual basis, the following interpretations can be drawn:

i. increasing temperature led to an increased density;
ii. plasma treatment conducted to a higher absorption as compared to conventional heating processing;
iii. a higher density means a lower porosity and a lower absorption; this explains the observed substantial dissimilarity (opposition) between the two groups, (A + P) and (T + ρ).

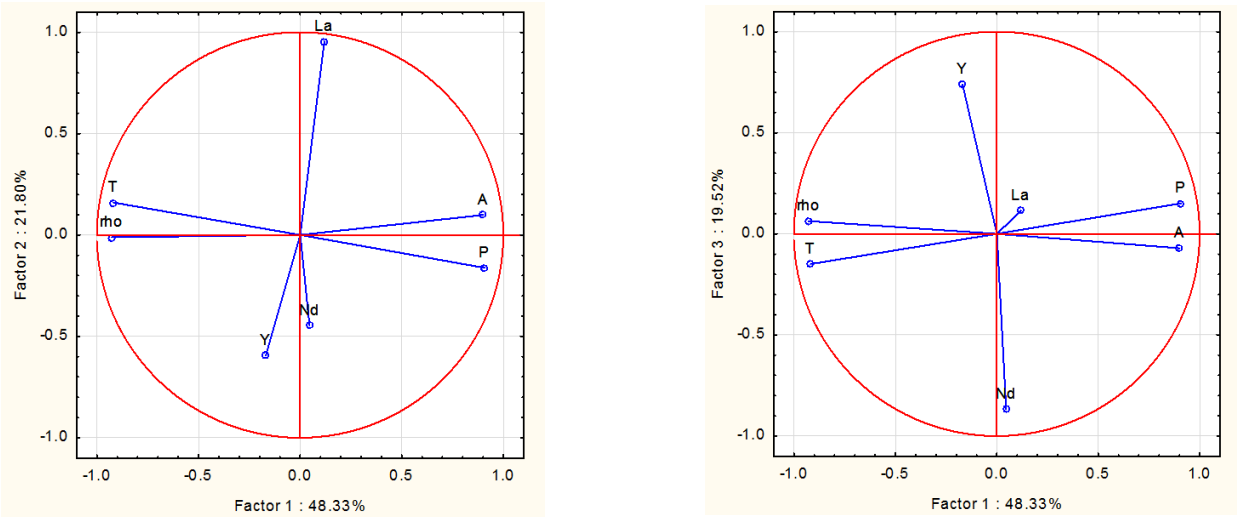

(**a**) (**b**)

Figure 2. Projection of the variables on (**a**) PC1 and PC2 plane; (**b**) PC1 and PC3 plane. The first three PCs strongly explain the data variability: 48.33 + 21.80 + 19.52 = 89.65%.

On PC2, which accounts for about 22% of the data variability, variables that strongly influenced PC 1: (A + P) and (T + ρ) had little or negligible influence as they were almost entirely involved in PC1. La is highly influential on PC2 (being close to the maximum, 1), while Y and Nd have a lower influence on PC2 (around 0.5) and opposite (negatively correlated) to La; they have a substantial effect of around 0.8 on PC3 (Figure 2b). That concludes that all the observations made in the analysis can explain, on a scientific basis, the behavior of the experimental results.

The analysis of the projections of the variables on the PC1 and PC2 plane in Figure 2a, coupled with the score plot in Figure 3 (observations are numbered according to Table 2, show useful data spreading patterns that can be interpreted as such as:

a. over PC1, right-handed data belong to the plasma (P) processed observations (29–42); they have high Absorption levels. For example, observations 29 and 30 have the highest Absorption among all, i.e., 36.61% and 38.71%;
b. observed projections on the plot's left side are controlled by (T + ρ). The higher the value of the projection on the PC, in absolute value, the stronger the influence of the corresponding variable.
c. over PC2, data placed on top (above PC1) are La_2O_3–doped Al_2O_3 while the ones below PC1 are Y_2O_3–doped Al_2O_3 and Nd_2O_3–doped Al_2O_3;
d. increasing doping ions lead to a higher projection of the scores on PC2 in absolute value. For example, but not only, score #30 corresponds to the alumina doped with 500 ppm La_2O_3, while score #29 has been doped with 1000 ppm La_2O_3.

Various-sized clusters can be identified in Figure 3; La, Nd + Y containing alumina and plasma processed materials are the three major ones. Note that clusters could overlap, for example, in the upper right quadrant, which means that observations 29–31 and 37–38 are plasma-processed and La-containing alumina. Smaller clusters were not graphically identified here, yet a visual inspection can easily detect them. Temperature and alumina sources can also play an important role in interpreting clusters.

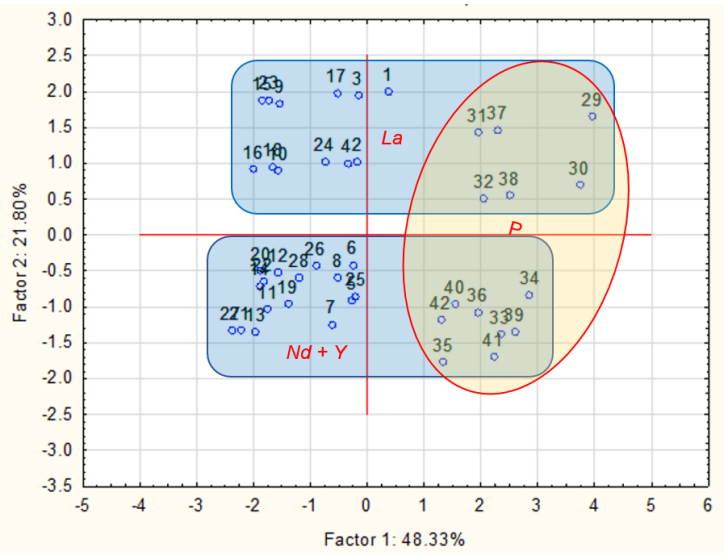

Figure 3. Projection of the scores on PC1 and PC2 plane. Several major and smaller clusters can be found.

3.3. Image Processing and Fractal Dimension Calculation

Several issues prevent one from accurately assessing and making comparisons of the microstructural features, for example, to obtain and compare particles' Shape Factors:

(a) microstructural features look different at different scales.
(b) compacted areas and regions showing well-defined grain boundaries could be found in the same image (see Figure 4d);
(c) fracturing process results, such as fracture planes and edges, can be found in some images.
(d) high intergranular porosity in some cases or compacted areas containing isolated pores (microporosity);
(e) artifacts.

Therefore, Fractal Dimension was chosen as the method to be used (as it does not require closed boundaries). It was computed for each image as a microstructural feature quantifier via two approaches in detecting edges in the image (and the results were evaluated), to correlate alumina source–composition–processing–microstructure–properties.

Fractal Dimensions of the 2 sets × 206 SEM images recorded at different scales of observation (from 5 to 500 μm), corresponding to the 42 cases given in Table 2, were calculated. The two sets were obtained using two edge detection tools, the Find Edges tool, and the Canny Edge Detector plugin; the results were compared to identify the best approach.

Find Edges Tool was first used in Figure 4a, giving an FD = 1.527, thick edges, and a noisy image—see Figure 4b. The Canny Edge Detection plugin (Gaussian kernel radius 2, low threshold 2.5, high threshold 7.5) was used for comparison, giving an FD = 1.332—see Figure 4c. The Median filter was also considered in processing the image to remove the existing noise before applying any edge detection technique-Figure 4d. Although noise was eliminated from the images processed with Median Filter applied, FD values decreased, and fainter images were obtained, suggesting that some information was lost in the process–Figure 4e,f, than in the case where no filters were used. It was found that the Median filter is a useful denoising technique, but during the noise removal phase, it also affects the edges with loss of information, which was confirmed in [32]. Consequently, it was learned that Canny Edge Detection (CED) with no filter applied (CED uses itself as a filter for removing noise) was a better approach than ImageJ's Find Edges old tool, in terms of quality, and is also a simple procedure.

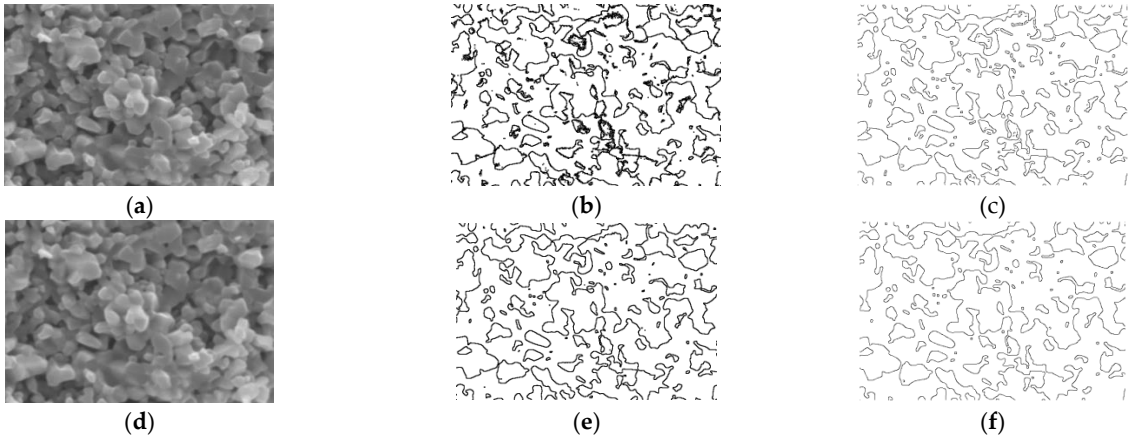

Figure 4. (**a**–**c**) A1La5 specimen processed at 1500 °C, scale 5 μm, no filter: (**a**) SEM image, (**b**) image obtained when Find Edges tool used, FD = 1.527, (**c**) when Canny Edge Detection plugin was used, FD = 1.332; (**d**–**f**) A1La5 specimen processed at 1500 °C, scale 5 μm, median filter applied: (**d**) softer SEM image with a certain loss of possible information, (**e**) when Find Edges tool was used on (**d**) image, FD = 1.447, (**f**) when Canny Edge Detection plugin was used on (**d**) image, FD = 1.291.

Whatever the processing procedure is used, with or without a median filter applied, it is essential to use the same technique for all images at different scales and with various structural features so that the results can be compared.

The steps of the image processing procedure are detailed and exemplified in Figures 5a–g and 6a–g, showing the different features existing in two SEM images obtained by using different dopants (La and Y oxides), with alumina from two different sources (A1 and A2), at different temperatures (1500 °C and 1815 °C) and, also, at different scales (50 μm and 10 μm, respectively). In addition to using different scales that make microstructure comparisons impossible/difficult, porosity and edges from fracturing made the thresholding procedure used in [10,16] unsuitable, as it will lead to loss of information, especially at smaller scales. Therefore, a simpler and yet effective procedure to obtain the edges and to compute the FD was used: (i) each image was cropped to exclude scale, magnification, data, etc.; (ii) images were converted to binary images (only white or black); (iii) Find Edges tool and Canny Edge Detector plugin were used to identify all edges (defined as being made of pixels that have a neighboring pixel of the other color); (iv) Fractal Box Count Tool based on Box Counting method allowed to obtain the Fractal Dimension.

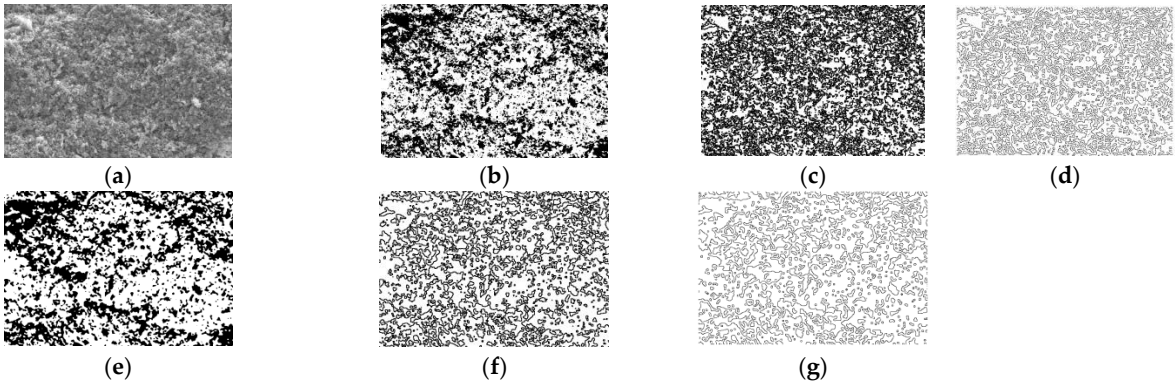

Figure 5. (**a**) SEM image of A1La5 processed at 1500 °C at scale: 50 μm; (**b**) image converted to binary; (**c**) detected edges (Find Edges tool) giving an FD = 1.887; (**d**) detected edges (Canny Edge Detection plugin) giving an FD = 1.717; (**e**) image converted to binary with the median filter applied, (**f**) detected edges median filter applied, FE tool, FD = 1.751; (**g**) detected edges, median filter applied, CED plugin, FD = 1.605.

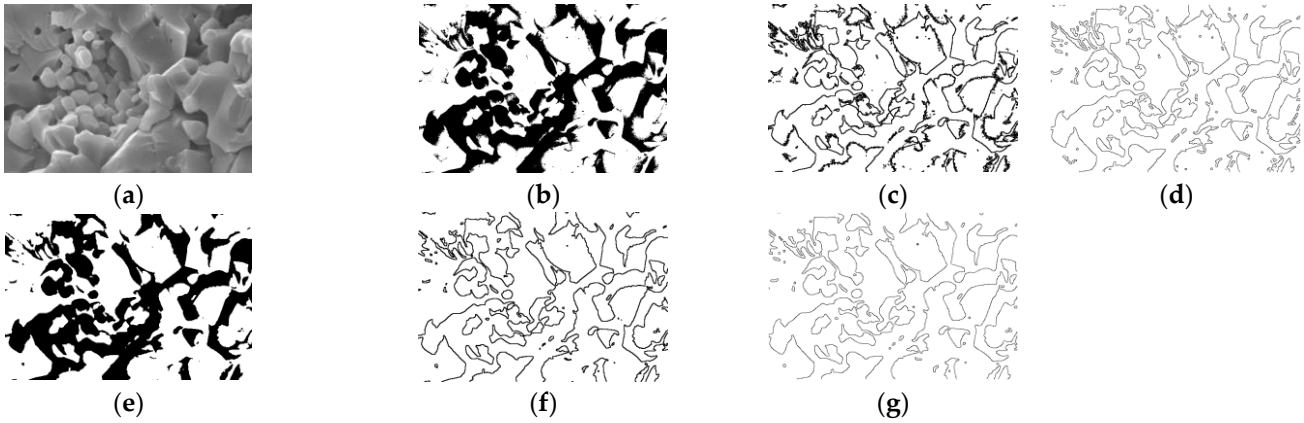

Figure 6. (**a**) SEM image of A2Y5 processed at 1815 °C at scale: 10 μm; (**b**) image converted to binary; (**c**) detected edges (Find Edges tool) giving an FD = 1.729; (**d**) detected edges (CED plugin) giving an FD = 1.318; (**e**) image converted to binary with the median filter applied, (**f**) detected edges median filter applied, FE tool, FD = 1.405; (**g**) detected edges, median filter applied, CED plugin, FD = 1.269 (image looks fainter than (**d**) image).

Results from processing all 206 micrographs with the two edge detection techniques were analyzed. Figure 7a–d shows the histograms of (a) A, (b) rho, (c) FD obtained by using the Find Edges tool, and (d) the Canny Edge Detector plugin. Absorption and Density were characterized by using the 42 cases data in Table 2, and fractal dimension was characterized by using the 206 cases corresponding to the 206 images available, processed successively with the Find Edges tool and Canny Edge Detector plugin. An abnormality was recorded for Absorption less than 5% (15 cases of 42); these cases were processed at high temperatures (1815 °C), were made from A3 alumina, and/or contained Y and Nd oxides in the highest concentrations. The same histogram also displays two cases isolated from the rest of the observations, belonging to plasma-processed specimens that have very high absorptions, around 38%. The fractal dimension obtained using the Find Edges tool has a significant departure from normality in the 1.9–2 bin due to the high noise and thick edges that resulted from using that tool. Density and Fractal dimension obtained by using Canny Edge Detector plugin showed almost normal distributions. Adding to the previous partial conclusions deduced by comparing the effectiveness of the two techniques, the Canny Edge Detection plugin gives more accurate results than the Find Edges tool to identify edges, providing more acceptable results with less noise.

3.4. PCA with Fractal Dimension Results

3.4.1. FD Computed with Find Edges Tool

Principal Component Analysis included Fractal Dimension values obtained from the 206 images processed with the Find Edges tool. FD obtained a high value close to Density and Temperature, Figure 8a, which is unrealistic; increasing temperature makes the structure more compact, so the FD should decrease as grains grow. The reason is that grain growth and dropping porosity at sintering lead to a decrease in the overall grain boundaries length; therefore, smaller FDs will be obtained. However, the scores plot, Figure 8b, grouped by index I (alumina type: I = 1, 2, 3) compared with the variables plot, reveals that alumina type I = 1 (A1 source) can be found only in the lower quadrants of the scores plot, which are controlled by La oxide. Doped alumina from alumina 2 and 3 can be found in all quadrants; lower quadrants contain La-doped alumina, while upper quadrants contain Y (in the left quadrant) and Nd-doped alumina (in the right quadrant).

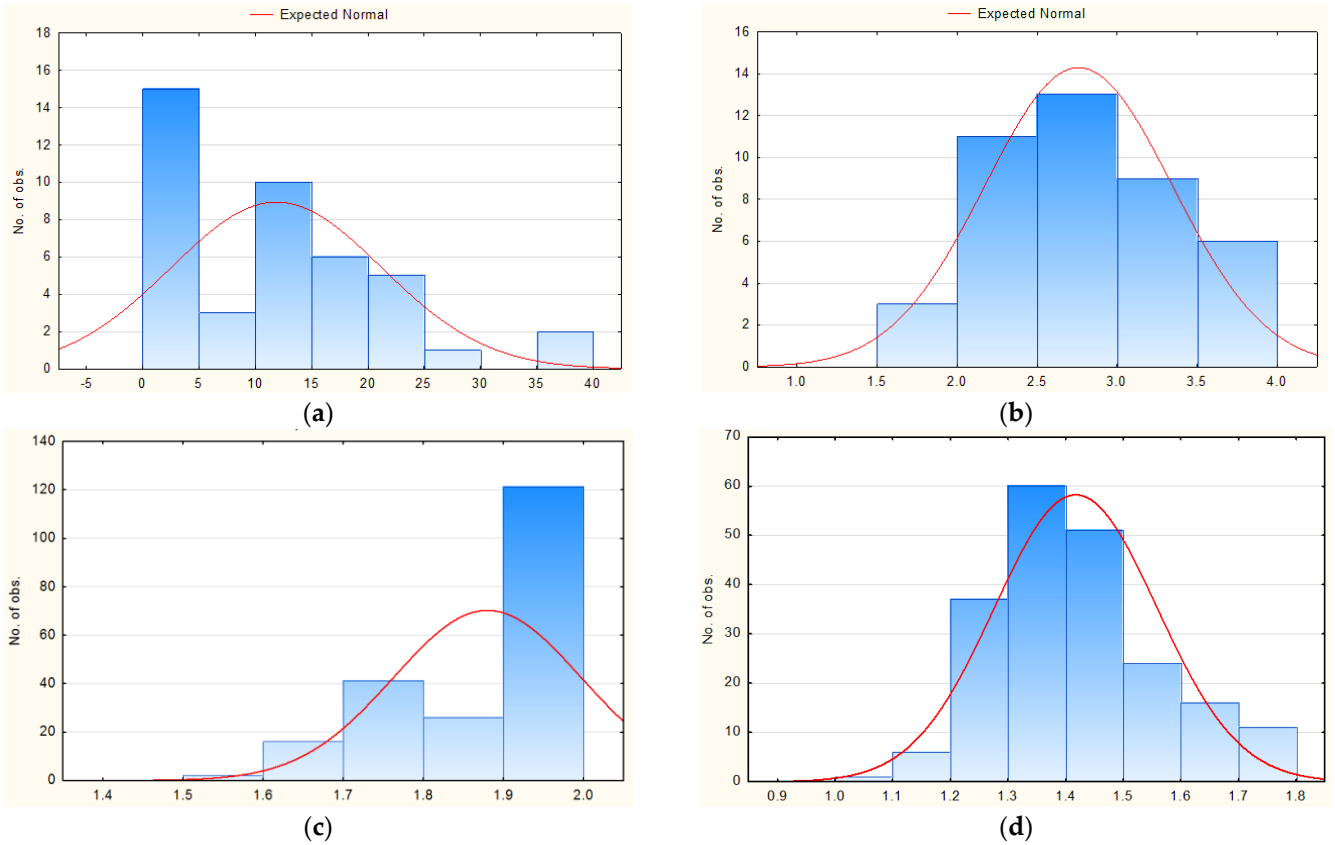

Figure 7. Histograms of (**a**) absorption; (**b**) density, and fractal dimension (**c**,**d**), obtained using (**c**) Find Edges tool and (**d**) the Canny Edge Detection plugin (K-S d ≅ 0.15, $p > 0.20$, Lilliefors $p < 0.05$).

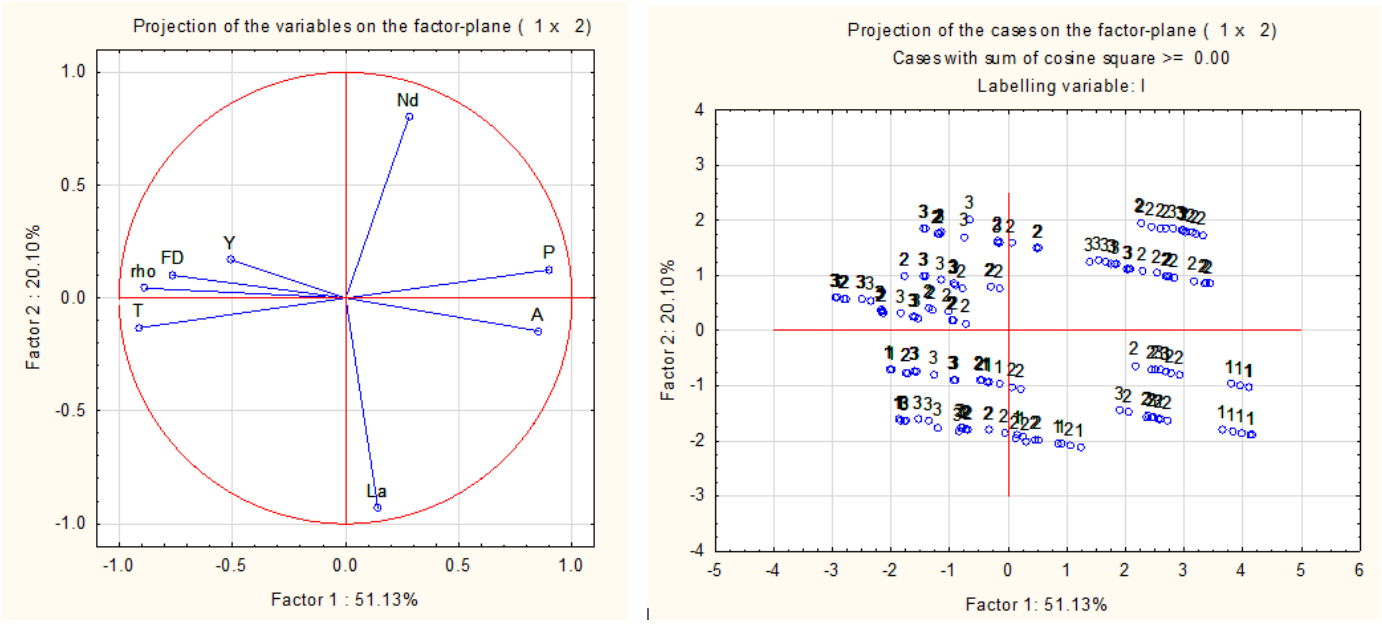

Figure 8. PCA including Fractal Dimension (FD) computed on images processed with the Find Edges tool; (**a**) variables plot, (**b**) Scores plot. Index I was used for grouping ceramics made from the A1–A3 alumina sources.

3.4.2. FD Computed with Canny Edge Detection

Further PCA tests were made on images processed with the Canny Edge Detection plugin. Relationships (similarities and dissimilarities) between observations and variables can be drawn, to a certain extent, by comparing scores and variables plots in Figure 9, pairs (a) and (b), (c) and (d), and pair (e) and (f). Well-clustered data can be observed in all plots, with a noticeable influence of the opposite relationship between FD and Y exerted on the clustering process of the observations in Figure 9, pair (e) and (f). Five major clusters, oriented along the FD-Y direction, have high FD values on their lower parts and lower values on their upper parts. For example, observation #23–A2La10_1500, scale 50 µm, FD = 1.666, is positioned in the lower part of the cluster; observation #154–A1La10_Plasma, scale 5 µm, FD = 1.249, is set in the upper part of the cluster; observation #96–A3La5_1500, scale 50 µm, FD = 1.733, is positioned in the lower part of the cluster; observation #148–A1La5_Plasma, scale 5 µm, FD = 1.262, is set in the upper part of the cluster, etc.).

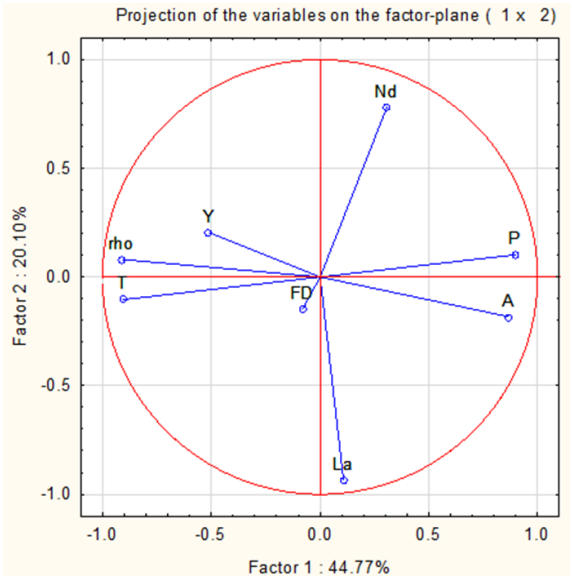

(**a**)

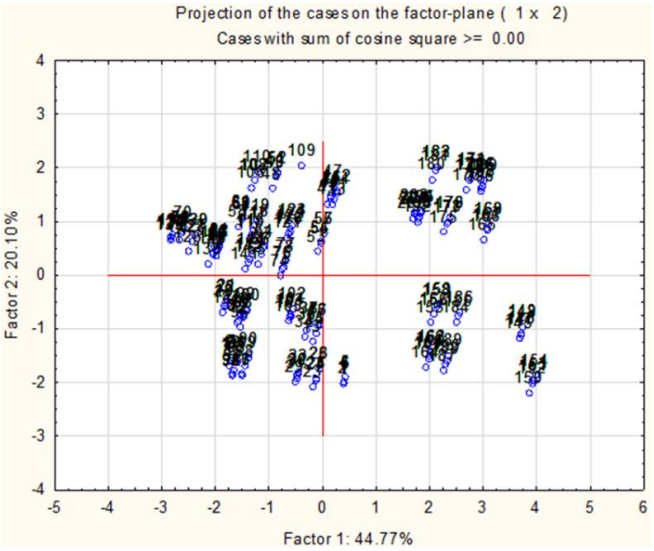

(**b**)

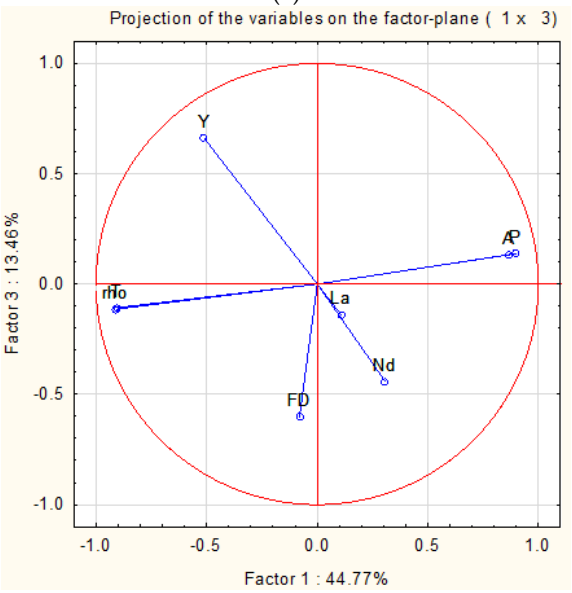

(**c**)

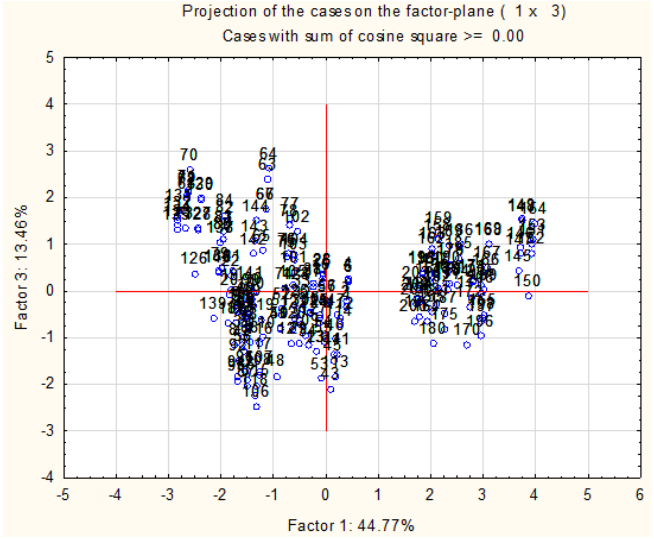

(**d**)

Figure 9. *Cont.*

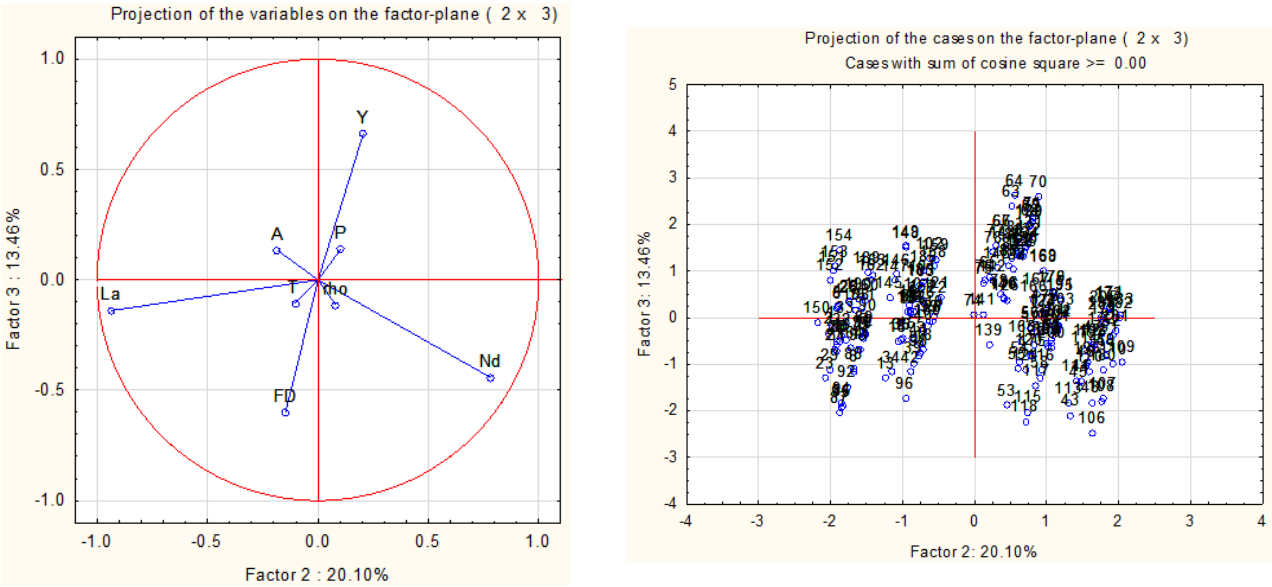

(**e**) (**f**)

Figure 9. PCA adding Fractal Dimension (FD) computed on images processed with Canny Detection plugin; (**a**) variables plot in PC1-PC2 projection plane, (**b**) Scores plot in PC1-PC2 projection plane, (**c**) variables plot in PC1-PC3 projection plane, (**d**) Scores plot in PC1-PC3 projection plane, (**e**) variables plot in PC2-PC3 projection plane, (**f**) Scores plot in PC2-PC3 projection plane. The amount of variability covered by the first 3 PCs in the data decreased to 78%.

A less obvious influence, at first glance of the Y and FD relationship, however, an existing one, can be observed for the pair Figure 9c,d on the two major clusters that extend almost vertically (in their lower parts) on the left quadrants (clusters' upper part is tilted to the left, following the Y vector direction). Lower-positioned observations, controlled by FD, correspond, also, to high FD values (for example, observations: #53–A2Nd5_1500, scale 5 µm, with an FD = 1.752; #106–A3Nd10_1500, scale 5 µm, with an FD = 1.669) while higher-positioned observations to high Y intakes (#64–A2Y10_1500, scale 50 µm with an FD = 1.269, #70–A2Y_1800, scale 10 µm with an FD = 1.183, etc.).

Figure 9a shows that, in the complex picture of the influences, FD is very close to the middle average point on the projection plane and properties are influenced, mainly, by the powerful T and P. However, it was revealed in Figure 9, pair (c) and (d), and pair (e) and (f) that FD has a noticeable influence over the observations' distribution, being correlated with La, Nd, and Y." While (T and ρ) and (A and P) explain the distribution of the observations horizontally in Figure 9d, along with Nd and La, FD and Y do the same on the (almost) vertical direction—see Figure 9d,f.

To increase visibility and make the analysis easier, PCA biplots (Figure 10a,b) were obtained. Figure 10a,b shows the existence of two major, well-defined clusters of observations (points in blue), one on the right and the other in the middle-to-left part of each biplot. Two major orientations can be identified: along the t1 direction (PC1), Temperature, Density, and Absorption are correlated, positively or negatively, especially in Figure 10a; along the t2 (PC2) direction, La, Nd, FD, and Y are strongly correlated. The ascending order for Absorption is from left to right and inversely for Temperature, Density, suggesting that Absorption is negatively correlated to Temperature and Density. Consequently, the cluster on the right has a higher Absorption than the left cluster, which, instead, has a higher Density, being processed and a higher Temperature.

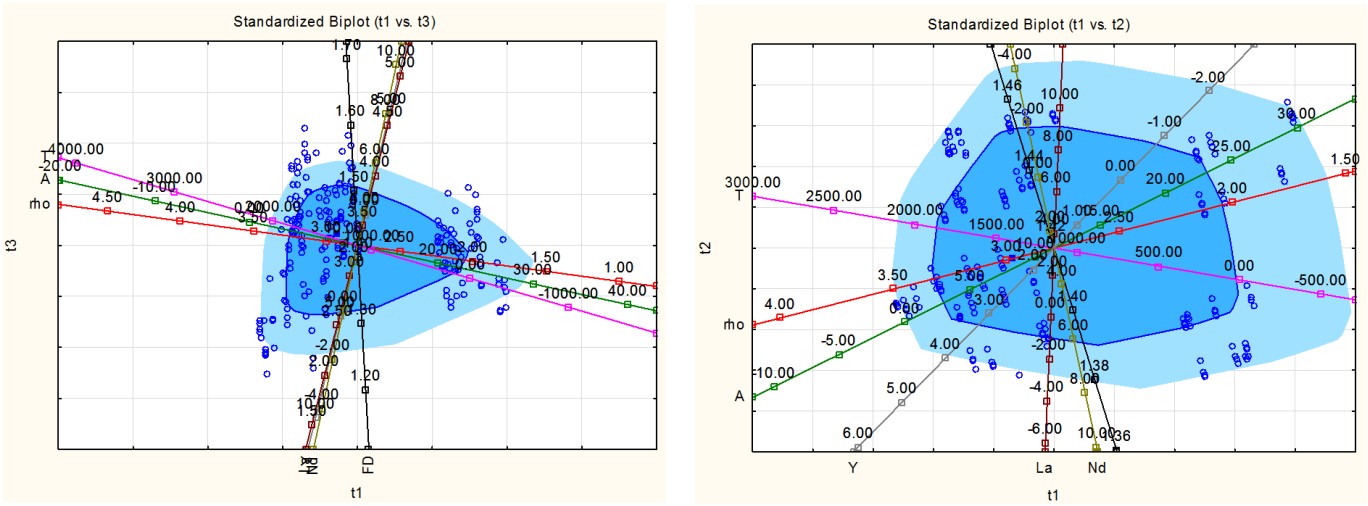

(**a**) (**b**)

Figure 10. PCA biplots on: (**a**) PC1 and PC3 projection plane; (**b**) PC1 and PC2 projection plane, (Note: missing label of the black axis is FD).

A quadratic model was used to fit ρ = *f(FD, A)*—see Figure 11a—and Equation (3) was derived. A strong correlation (R^2 = 0.88) resulted, primarily due to the excellent correlation ρ = *f(A)*, which has an R^2 = 0.94. Most of the data is well fitted by the resulting surface; however, five outliers were found—see Figure 11b—having residuals of negative 0.8–0.9, all belonging to A3Y5, plasma-processed results. The explanation is A3Y5 has an abnormal Absorption of only 5.16%; the 5 outliers correspond to the 5 A3Y5 micrographs taken at various scales. These outliers are the same as the points that have a significant departure from the regression surface in Figure 11a.

$$\rho = 3.9455 - 0.8513 \cdot FD - 0.0670 \cdot A + 0.4171 \cdot FD^2 - 0.0137 \cdot FD \cdot A + 0.0009 \cdot A^2 \quad (3)$$

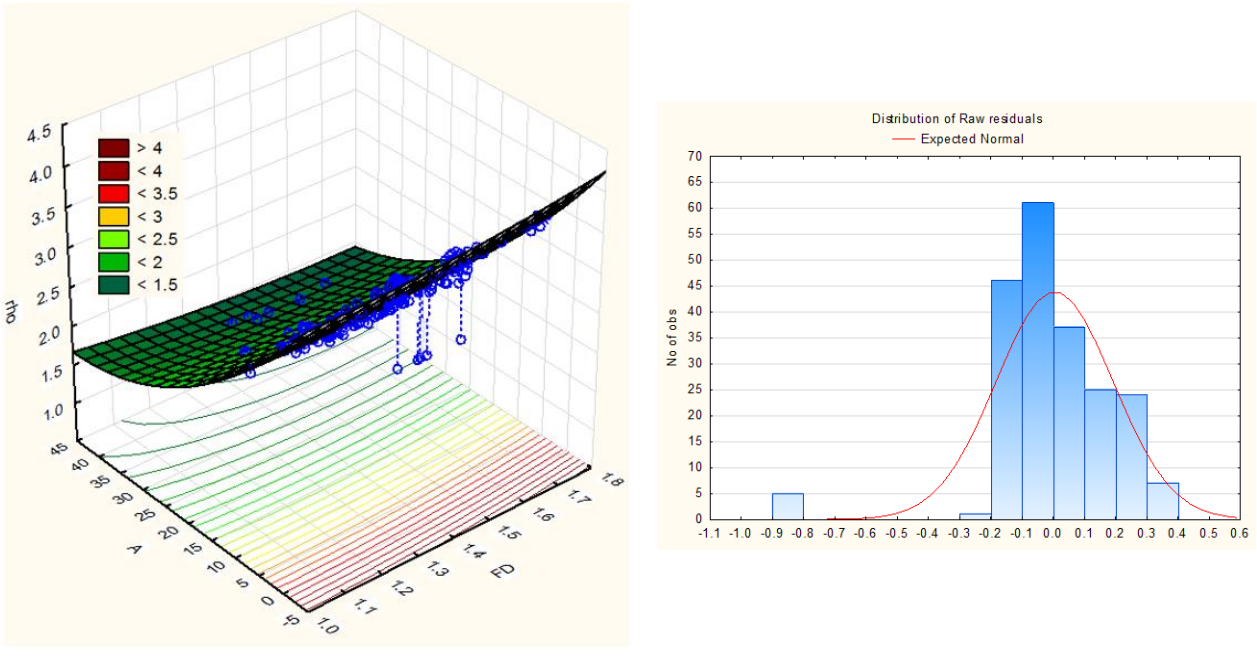

(**a**) (**b**)

Figure 11. (**a**) Regression surface from fitting ρ = f(*FD*, *A*) with a quadratic model (resulted in R^2 = 0.88); (**b**) Residuals recorded by using the derived Equation (3) resulting from fitting.

4. Conclusions

A comprehensive statistical analysis was successfully completed for drawing strong and accurate correlations in the causal chain: materials–composition–processing–microstructure–properties, by using various choices for each link of this chain. Alumina ceramics from three different alumina sources doped with three rare-earth oxides were employed in the sintering process through three different heating methods. Ceramic properties were measured, resulting in a complex, multivariate database. Principal Component Analysis helped interpret the data well and useful correlations were extracted. All links, nature of alumina source, dopants, concentration levels, processing conditions (firing temperatures, plasma processing), microstructural features, and ceramic properties were found to be significant and correlated in the multivariate analysis. To quantify the microstructural features, 206 SEM micrographs were recorded at various scales, and the corresponding images were processed. Two edge detection techniques were used; Fractal Dimension (FD) was calculated for each micrograph, and results were compared. The fractal dimension was effective in quantifying highly dissimilar and/or noisy microstructures, such as was the case here, and played a pivotal role in that chain of correlations. Comparisons of the FD obtained using two edge detection techniques, ImageJ's Find Edges tool and Canny Edge Detection plugin, allowed us to select the last one, the CED plugin, to be the best option in terms of quality and processing effort. Properties Density and Absorption were found to be strongly correlated to processing conditions (Temperature and Plasma processing). Fractal Dimension was correlated to Y, Nd, and La, helping to explain the distribution of the observations, i.e., the influence of the composition. Also, a strong correlation $\rho = f(FD, A)$ was identified.

Author Contributions: Conceptualization, Z.D.G. and A.V.; methodology, Z.D.G. and A.V.; validation, E.V.; investigation, Z.D.G., A.V. and E.V.; writing—original draft preparation, Z.D.G. and A.V. All authors have read and agreed to the published version of the manuscript.

Funding: This research received no external funding.

Data Availability Statement: The data presented in this study are available on request from the corresponding author.

Conflicts of Interest: The authors declare no conflict of interest.

References

1. Wang, D.; Mei, H.; Liu, L.; Zhang, J. The effect of heating rate on sintering mechanism of alumina nanoparticles. *J. Am. Ceram. Soc.* **2022**, *105*, 7149–7158. [CrossRef]
2. Shigeno, K.; Kuraoka, Y.; Asakawa, T.; Fujimori, H. Sintering mechanism of low-temperature co-fired alumina featuring superior thermal conductivity. *J. Am. Ceram. Soc.* **2021**, *104*, 2017–2029. [CrossRef]
3. Ghorbel, I.; Ganster, P.; Moulin, N.; Meunier, C.; Bruchon, J. Direct microwave heating of alumina for different densities: Experimental and numerical thermal analysis. *J. Am. Ceram. Soc.* **2023**, *106*, 2773–2785. [CrossRef]
4. Fang, J.; Thompson, A.M.; Harmer, M.P.; Chan, H.M. Effect of Yttrium and Lanthanum on the Final-Stage Sintering Behavior of Ultrahigh-Purity Alumina. *J. Am. Ceram. Soc.* **1997**, *80*, 2005–2012. [CrossRef]
5. Cho, J.; Harmer, M.P.; Chan, H.M.; Rickman, J.M.; Thompson, A.M. Effect of yttrium and lanthanum on the tensile creep behavior of aluminum oxide. *J. Am. Ceram. Soc.* **1997**, *80*, 1013–1017. [CrossRef]
6. DeLellis, D.P.; Mecholsky, N.A.; Mecholsky, J.J., Jr.; Quinn, G.D. A fractal analysis of crack branching in borosilicate glass. *J. Am. Ceram. Soc.* **2020**, *103*, 5283–5290. [CrossRef]
7. Penilla, E.H.; Devia-Cruz, L.F.; Duarte, M.A.; Hardin, C.L.; Kodera, Y.; Garay, J.E. Gain in polycrystalline Nd-doped alumina: Leveraging length scales to create a new class of high-energy, short pulse, tunable laser materials. *Light Sci. Appl.* **2018**, *7*, 33. [CrossRef]
8. Bodisová, K.; Klement, R.; Galusek, D.; Pouchly, V.; Drdlíkc Maca, K. Luminescent rare-earth-doped transparent alumina ceramics. *J. Eur. Ceram. Soc.* **2016**, *36*, 2976. [CrossRef]
9. Terzi, M. Particle size distribution analysis in aggregate processing plants using digital image processing methods. *Rev. Romana Mater/Rom. J. Mater.* **2018**, *48*, 514–521.
10. Ghizdăveț, Z.; Năstac, D.; Eftimie, M.; Stanciu, I.; Volceanov, A. Correlations composition-processing-microstructure on some clinkers. Implications. *Rev. Romana Mater/Rom. J. Mater.* **2016**, *46*, 453–464.
11. Podczeck, F. A shape factor to assess the shape of particles using image analysis. *Powder Technol.* **1997**, *93*, 47–53. [CrossRef]

12. Petcu, G.; Dobrescu, G.; Atkinson, I.; Ciobanu, M.; Blin, J.-L.; Parvulescu, V. Evolution of Morphology, Fractal Dimensions, and Structure of (Titanium) Aluminosilicate Gel during Synthesis of Zeolites Y and Ti-Y. *Fractal Fract.* **2022**, *6*, 663. [CrossRef]
13. Chen, C.; Ding, X.; Wang, Y.; Luo, Z.; Zhai, P. Fractal Dimension Analysis of Structure and Bending Strength of Porous Alumina Prepared Using Starch and Carbon Fiber as Pore-Forming Agents. *Fractal Fract.* **2022**, *6*, 574. [CrossRef]
14. Mahovic Poljacek, S.; Risovic, D.; Furic, K.; Gojo, M. Comparison of fractal and profilometric methods for surface topography characterization. *Appl. Surf. Sci.* **2008**, *254*, 3449–3458. [CrossRef]
15. Milosevic, N.T.; Jelinek, H.F.; Rasjkovic, N.; Ristanovic, D. Richardson's method of segment counting versus box-counting. In Proceedings of the 19th International Conference on Control Systems and Computer Science, Bucharest, Romania, 29–31 May 2013; IEEE: Washington, DC, USA. [CrossRef]
16. Ghizdavet, Z.; Stanciu, I.M.; Melinescu, A.; Ianculescu, A. Correlations composition-processing–microstructure-properties for ceria-based solid electrolytes. *Rev. Chim-Buchar.* **2017**, *68*, 1044–1050. [CrossRef]
17. Husain, A.; Reddy, J.; Bisht, D.; Sajid, M. Fractal dimension of coastline of Australia. *Sci. Rep.* **2021**, *11*, 6304. [CrossRef] [PubMed]
18. Akkari, H.; Bhourib, I.; Dubois, P.; Bedoui, M.H. On the Relations Between 2D and 3D Fractal Dimensions: Theoretical Approach and Clinical Application in Bone Imaging. *Math. Model. Nat. Phenom.* **2008**, *3*, 48–75. [CrossRef]
19. Li, L.; Li, Z.; Mingli, C.; Tang, Y.; Zhang, Z. Nanoindentation and porosity fractal dimension of calcium carbonate whisker reinforced cement paste after elevated temperatures (up to 900 °C). *Fractals* **2021**, *29*, 2140001-13. [CrossRef]
20. Manukovskaya, D.V.; Sidorov, N.V.; Starodub, O.R.; Palatnikov, M.N. Fractal Analysis of Photoinduced Light Scattering Pictures in Stoichiometric Lithium Niobate Single Crystals. *Ferroelectrics* **2014**, *473*, 100–109. [CrossRef]
21. State, R.; Volceanov, A.; Volceanov, E.; Stoleriu, S. Alumina composites obtained by unconventional heat treatment. *Rev. Romana Mater/Rom. J. Mater.* **2011**, *48*, 514–521.
22. Lever, J.; Krzywinski, M.; Altman, N. Principal component analysis. *Nat. Methods* **2017**, *14*, 641–642. [CrossRef]
23. Jolliffe Ian, T.; Cadima, J. Principal component analysis: A review and recent developments. *Philos. Trans. R. Soc. A* **2016**, *374*, 2015020220150202. [CrossRef] [PubMed]
24. Ghizdavet, Z.D.; Ștefan, B.M.; Nastac, D.; Vasile, O.; Bratu, M. Sound absorbing materials made by embedding crumb rubber waste in a concrete matrix. *Constr. Build. Mater.* **2016**, *124*, 755–763. [CrossRef]
25. StatSoft EUROPE. Available online: https://www.statistica.com/en/ (accessed on 13 March 2023).
26. University of Auckland, New Zeeland. Available online: https://www.cs.auckland.ac.nz/courss/compsci373s1c/PatricesLectures/Image%20Filtering.pdf (accessed on 19 February 2023).
27. ImageJ. Image Processing and Analysis in Java. Available online: https://imagej.nih.gov/ij/docs/menus/process.html (accessed on 19 February 2023).
28. OpenSource Computer Vision. Available online: https://docs.opencv.org/4.x/da/d22/tutorial_py_canny.html (accessed on 20 February 2023).
29. O'Donnell, R.G. An Investigation of the Fragmentation Behaviour of Impacted Ceramics. *J. Mater. Sci. Lett.* **1991**, *10*, 685–688. [CrossRef]
30. Sherman, D.; Brandon, D.G. The Ballistic Failure Mechanisms and Sequence in Semi-Infinite Supported Alumina Tiles. *J. Mater. Res.* **1997**, *12*, 1335–1343. [CrossRef]
31. Yoshida, H.; Ikuhara, Y.; Sakuma, T. High-temperature creep resistance in rare-earth-doped, fine-grained Al_2O_3. *J. Mater. Res.* **1998**, *13*, 2597–2601. [CrossRef]
32. Verma, K.; Singh, B.K.; Thoke, A.S. An Enhancement in Adaptive Median Filter for Edge Preservation. *Procedia Comput. Sci.* **2015**, *48*, 29–36. [CrossRef]